Nanoscale

Volume 1 | Number 1 | Jan 2013 | Pages 1–100

Nanoscale

www.rsc.org/nanoscale

ROYAL SOCIETY OF CHEMISTRY

ROYAL SOCIETY OF CHEMISTRY

www.rsc.org/nanoscale

Journal Name

ARTICLE

Crossed Ferric Oxide Nanosheets Supported Cobalt Oxide on 3-Dimensional Macroporous Ni Foam Substrate Used for Diesel Soot Elimination under Self-Capture Contact Mode

Chunmei Cao[a], Xingang Li*[a], Yuqing Zha[a], Jing Zhang[b], Tiandou Hu[b] and Ming Meng*[a]

Crossed Fe_2O_3 nanosheets supported cobalt oxide nanoparticles on three-dimensionally macroporous nickel foam substrate (xCo/Fe-NF) were designed and successfully prepared through a facile hydrothermal and impregnation route. These catalysts showed high catalytic soot combustion acivities under self-capture contact mode. The three-dimensional macroporous structures of Ni foam and the crossed Fe_2O_3 nanosheets constituted macroporous "little rooms" can greatly increase contact efficiency between soot particulates and catalysts. The interaction between Co and Fe facilitated the activation of Fe-O bond and increased the amounts of active oxygen species, thus improving the redox property of the catalysts. The 0.6Co/Fe-NF catalyst exhibited the highest turnover frequency (TOF) for soot combustion, which is in good accordance with the largest amount of active oxygen species. Based upon the catalytic performance and multiple characterization results, two reaction pathways for soot oxidation are identified, namely, the direct oxidation by the activated oxygen species via oxygen vacancies and the NOx-aided soot oxidation.

1 Introduction

Soot particulates released from diesel engines are doing great harm on human bodies and atmospheric environment.[1, 2] So, it is urgent to restrict the emission of soot particulates. At present, the most effective and promising technology for diesel soot particulates after-treatment is the combination of diesel particulate filters (DPF) and oxidation catalysts.[3-8] In such combination systems, catalysts coated on the filters must possess high soot oxidation activity and high thermal stability under practical working conditions.[9] It is known that the catalytic oxidation of soot particulates is a gas-solid-solid triple-phase reaction which contains the gaseous reactants (oxygen and/or NOx), solid soot particulates and solid catalyst, which determines the complexity of this reaction system. In addition to the intrinsic activity of catalysts, the contact efficiency (the number of contact points) between soot particulates and catalysts also significantly influences the performance of the catalysts for soot oxidation.[10] Since soot

particulates often have large size (25~100 nm), they can hardly enter the inner surface of micropores and mesopores, leading to very low contact efficiency between soot and catalytic sites, as a result, the soot oxidation rate is greatly decreased. To further improve the catalytic oxidation activity of conventional catalysts, researchers are always endeavoring to upgrade the catalysts from the following three aspects: (1) modification of catalyst compositions in order to increase the intrinsic activity of the catalysts;[11-15] (2) improvement of the specific surface area of the catalysts in order to increase the dispersion of active phase and increase the tangible active sites between reactants and catalysts;[2, 16, 17] (3) design and synthesis of macroporous catalytic materials in order to increase the contact efficiency between soot and catalysts.[18, 19] Several studies have reported that three-dimensionally ordered macroporous (3DOM) catalysts can exhibit much higher catalytic activity for soot oxidation than conventional microporous or mesoporous catalysts due to the greatly improved soot-catalyst contact efficiency.[20-22] Meanwhile, our group has found that many kinds of one-dimensionally nanoarray oxide catalysts such as nanorods, nanotubes and nanobelts arrays on two-dimensional substrate can also remarkably increase the soot-catalyst contact points and catalytic efficiency under a loose contact mode called gravitational contact mode (GCM).[5, 7, 23, 24] However, the employed two-dimensional substrates such as metal plates are airtight, which is unfavorable to the transfer of reactants during reactions; in addition, since mixed or complexed ox

[a]Collaborative Innovation Center of Chemical Science and Engineering (Tianjin), Tianjin Key Laboratory of Applied Catalysis Science & Engineering, School of Chemical Engineering & Technology, Tianjin University, Tianjin 300072 (P. R. China). E-mail: Xingang_li@tju.edu.cn; Fax: +86 22-2789-2275
[b]Beijing Synchrotron Radiation Facility, Institute of High Energy Physics, Chinese Academy of Sciences, Beijing 100049, P. R. China
† Electronic Supplementary Information (ESI) available: The images of HRTEM, EDS mapping, SEM, EXAFS and Fe 2p XPS. The table providing information on prepared catalysts. See DOI: 10.1039/x0xx00000x

nanoarray catalysts can hardly be synthesized, the reported nanoarray catalysts always consisted of pure single oxides, such as CuO, Co_3O_4 or CeO_2; the absence of other promoters or active components limited their catalytic activity and decreased their thermal stability, either. Therefore, further modification of as-reported single-oxide nanoarray catalysts obtained on two-dimensional airtight substrate is still rather necessary.

As known, nickel foam is a three-dimensional macroporous (3DM) material which has been widely employed in electrochemistry and heterogeneous catalysis as a substrate material.[25-32] By using the interconnected macroporous structure of nickel foam the contact chance between soot particulates and catalysts could be remarkably improved, and the mass transfer could also be facilitated; however, the nickel oxide itself exhibited very limited catalytic oxidation activity for soot combustion. To solve this problem, crossed Fe_2O_3 nanosheets were synthesized on nickel foam (Fe-NF), which can provide new macroporous structures between crossed sheets. In order to further increase the activity, cobalt oxide nanoparticles with adjustable content was supported on the crossed Fe_2O_3 nanosheets (xCo/Fe-NF, x=0.3, 0.6 and 0.9, x/100 represents the mass percentage of Co element in the catalyst). The final catalysts displayed uniform crossed nanosheets structure (sheet thickness: ~17.1 nm) which well distributed on the nickel foam. Under a simple and feasible loose contact mode called self-capture contact mode (SCCM) they exhibited particularly high catalytic performance for soot combustion, especially the sample 0.6Co/Fe-NF. The high performance could be attributed to the increased soot-catalyst contact efficiency in such special macroporous structure and the improved physical-chemical properties of the catalysts. Based on SEM, TEM, XRD, XANES, XPS, soot-TPR characterization results and the calculated TOF values, the correlation between the structures and catalytic performance for this macroporous catalytic system was clearly revealed, and two reaction pathways for soot oxidation namely the direct oxidation by the activated oxygen species via oxygen vacancies and the NOx-aided soot combustion were identified.

2 Experimental

2.1 Synthesis of Fe_2O_3 nanosheets on nickel foam (Fe-NF)

Firstly, a piece of nickel foam (about 2.5 cm × 5 cm) was cleaned with 2 M HCl in a ultrasound bath for 5 min in order to remove the surface NiO layer; then it was washed with deionized water and absolute ethanol for 5 min, respectively. Fe_2O_3 nanosheets on the nickel foam were synthesized by a simple hydrothermal method. In a typical procedure, 1.5 mmol of $Fe(NO_3)_3 \cdot 9H_2O$ and 7.5 mmol of $CO(NH_2)_2$ were dissolved in 50 mL water. After slight stirring for 30 min, the mixture solution was transferred into Teflon-lined stainless steel autoclaves. Subsequently, a piece of cleaned nickel foam was immersed into the reaction solution. The autoclave was sealed and maintained at 120 °C for 12 h and allowed to cool down to

room temperature naturally. After the reaction, the substrate was taken out and rinsed with distilled water and ethanol for three times, respectively, which was successively dried at 60 °C in a drying oven, and calcined at 500 °C in a muffle furnace in air for 2 h to get the final sample, denoted as Fe-NF.

2.2 Preparation of xCo/Fe-NF catalysts

The Fe-NF supported cobalt oxide catalysts with adjustable Co content (denoted as xCo/Fe-NF, x=0.3, 0.6 or 0.9, x/100 represents the mass percentage of Co element in the catalyst) were prepared by a simple wet impregnation method. Typically, the obtained Fe-NF was immersed into 0.1M, 0.5M and 0.7M $Co(NO_3)_2$ aqueous solution for 30 min, respectively. After being dried at 120 °C for 12 h in a drying oven, the as-prepared precursors were calcined in a muffle furnace at 500 °C in air for 2 h to get the final xCo/Fe-NF catalysts. By using inductively coupled plasma (ICP) method (Vista MPX instrument), the mass percentages (cobalt mass to the total sample mass) in different samples were about 0.3%, 0.6% and 0.9%, which corresponded to the used aqueous solutions of 0.1 M, 0.5 M and 0.7 M $Co(NO_3)_2$, respectively.

2.3 Preparation of the pure Ni foam catalyst as a reference

For comparison, the pure Ni foam catalyst was synthesized by calcining the cleaned nickel foam at 500 °C for 2 hours in a muffle furnace.

2.4 Characterization

The scanning electron microscopy (SEM) images of the catalysts were obtained on a field emission scanning electron microscope (a Hitachi S-4800) using an accelerating voltage of 3 kV. The transmission electron microscopy (TEM) and high resolution transmission electron microscopy (HRTEM) images were obtained on a JEOL JEM 2100F system using an accelerating voltage of 200 kV.

The X-ray diffraction patterns (XRD) of the products were recorded with Bruker D8 diffraction meter using Cu Kα (λ= 0.15418 nm) as radiation source.

The spectra of X-ray absorption near-edge structures (XANES) of the catalysts were recorded on Beijing Synchrotron Radiation Facility (BSRF) operating at ~150 mA and ~2.2 GeV. The X-ray absorption spectra of Co *K*-edge and Fe *K*-edge of the samples were recorded in fluorescence mode and those for reference compounds were recorded in transmission mode.

The X-ray photoelectron spectra (XPS) were recorded on a PHI-1600 ESCA spectrometer using Mg K_α radiation (1253.6 eV) as X-ray source. The binding energy was calibrated with C1s peak (B.E=284.6 eV) as standard and quoted with a precision of ±0.2 eV. The atomic composition of the samples at the surface was calculated.

The soot-TPR was carried out on a Thermo-Finnigan TPDRO 1100 instrument and the compositions of the effluent gas was analyzed with a HIDEN HPR20 mass spectrometer, by monitoring the signal of m/z=44 (CO_2). The mixture of soot and

catalyst was heated from room temperature to 900 °C at a heating rate of 10 °C min^{-1} in an atmosphere of N_2 with a flow rate of 50 mL min^{-1}.

2.5 Activity evaluation

The temperature-programmed oxidation (TPO) of soot was used to evaluate the catalytic activity of the prepared catalysts, using a fixed-bed tubular quartz reactor (Ø=8 mm). The Printex-U purchased from Degussa was used as the model soot. The self-capture contact mode (SCCM) was employed to achieve loose contact between the catalyst and soot, in which 6 mg of soot was dispersed in 20 mL ethanol under ultrasonic assistance; then catalysts 250 mg (including 10 mg of Fe_2O_3 crossed nanosheets and cobalt oxides nanoparticles) were immersed in the prepared suspension for the different periods (1 h, 6 h, 12 h, 18 h, 24 h and 48 h) during which the catalysts captured the soot particulates naturally through gravity deposition and adsorption; finally the mixture was dried at 60 °C for 2 hour and weighed. We chose the sample after the immersing 24 h for the followed tests, according to the desired soot loading (1 mg), i.e. the ratio value of soot and catalysts is 1/10 in weight. In each measurement, the mixture of soot and catalyst was heated from 200 to 650 °C at a heating rate of 2 °C min^{-1} in the flow 300 ppm NO and 5% O_2 balanced by N_2 (50 mL min^{-1}). The compositions of the effluent gas were analyzed by an on-line gas chromatograph (BFS, SP-3430) using a flame ionization detector (FID). The catalytic activity was evaluated by the values of T_{10} and T_{50}, which corresponded to the temperatures at the soot conversions of 10% and 50%, respectively. The CO_2 selectivity (S_{CO2}) was defined as $S_{CO2} = C_{CO2} / (C_{CO} + C_{CO2})$.

2.6 Isothermal kinetic measurement

The intrinsic activity of the catalysts based on the TOF value was defined as the ratio of the reaction rate to the active site amount of the catalysts. Isothermal soot combustion was performed at 330 °C, in which a low and stable conversion of soot (< 15%) was achieved in an approximate kinetic regime. At the total flow rate of 150 mL/min, no external mass transport limitations were detected. Meanwhile, the intraparticle mass transport limitations were also excluded by using small catalyst particles with the diameter less than 40 μm. The reaction rate (v) and the specific reaction rate normalized by unit BET surface area (v*) for soot combustion were calculated according to the following equations:[33]

$$v = - dn / mdt = CO_2 \times Q_c / m \qquad (1)$$
$$v^* = v / s = CO_2 \times Q_c / mS \qquad (2)$$

Where Q_c is the molar flow rate of gases through the reactor (mol/s), CO_2 is the measured molar fraction of these species in the gas phase, m is the mass of the catalyst (g), and S is the BET surface area of the catalyst (m^2/g).

The active sites density of catalysts was calculated by isothermal anaerobic titrations at the reaction temperature with soot as the probe molecule, which has been shown to be an accurate technique for quantifying active redox site

densities in metal oxide catalysts.[22, 34] When the concentration of CO_2 reached a stable level during the isothermal experiments, O_2 was instantaneously removed from the reactant stream. The transient decay in concentrations from steady state was monitored with an online gas chromatograph. To avoid the influence of the residual oxygen, the distance between the reactor and the detector was as small as possible. Before experiments, the samples were carefully calibrated with standard gas. The number of active redox sites available to soot under these reaction conditions can be quantified by integrating the diminishing rate of CO_2 formation with time:[33]

$$O^* \text{ amount (mol/g)} = 2P_0V \times A \times 10^{-6} / RTm \qquad (3)$$
$$O^* \text{ density (nm}^{-2}) = O^* \text{ amount} \times 6.02 \times 10^{23} / (S \times 10^{18}) \qquad (4)$$

Where P_0 is the atmospheric pressure (Pa), V is the volumetric flow rate of gases through the reactor (m^3/s), A is the integrated area of CO_2 concentration as a function of time (s), m is the mass of the catalyst (g), R is the ideal gas constant, T is the room temperature (K), and S is the BET specific surface area of the catalyst (m^2/g).

3 Results and discussion

The X-ray diffraction patterns of the catalysts Fe-NF, xCo/Fe-NF and reference sample Ni foam are presented in Fig. 1. From Fig. 1(A), the metallic Ni (JPCDS 04-0850) is identified as the main phase, although a little NiO (JPCDS 47-1049) is also observed for all the samples. While for the catalysts Fe-NF and xCo/Fe-NF, there are three weak peaks associated with Fe_2O_3 appearing at 30.2 °, 35.6 ° and 57.2 ° (JPCDS 39-1346), among which the one at 35.6 ° is enlarged and displayed in Fig. 1(B). However, for Co-containing catalysts xCo/Fe-NF, no diffraction peaks related to cobalt species appear, probably due to the low content of cobalt species and their high dispersion in Fe_2O_3 nanosheets.[23] To verify the existence of cobalt species, the X-ray absorption near-edge structure spectra (XANES) were recorded as shown in Fig. 2. It is obvious that the XANES spectra of the 0.3Co/Fe-NF are similar to that of the spinel $CoFe_2O_4$ with the main absorption peak (1s → 4p) appearing at ~7728 eV.[35] With the increase of supported cobalt species, the main absorption peaks of 0.6Co/Fe-NF and 0.9Co/Fe-NF shift to higher energy positions and gets closer to the main absorption peak of Co_3O_4 at ~7729 eV. In addition, a pre-edge absorption peak appearing at ~7708 eV is observed, which is assigned to a dipole-forbidden 1s → 3d transition. For quantitative analysis of different cobalt species, the linear combination fitting was performed, the results of which are listed in Table S1. Clearly, the cobalt species in the 0.3Co/Fe-NF catalyst exist as $CoFe_2O_4$, while those in the 0.6Co/Fe-NF and 0.9Co/Fe-NF mainly exist as the mixed phases of $CoFe_2O_4$ and Co_3O_4. With the increase of Co content, the ratio of Co_3O_4 increases.
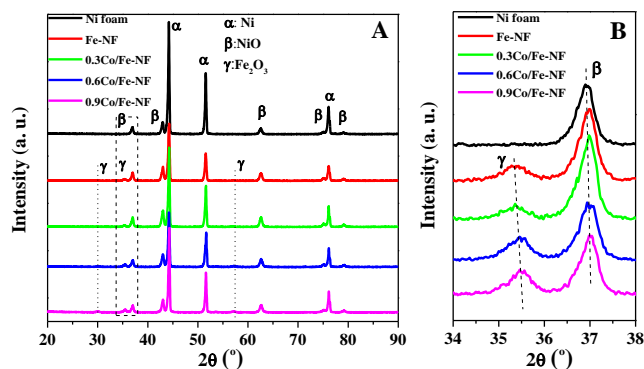
Fig. 1 The X-ray diffraction patterns of the Ni foam, Fe-NF and xCo/Fe-NF: (A) full patterns; (B) the regional enlarged patterns.
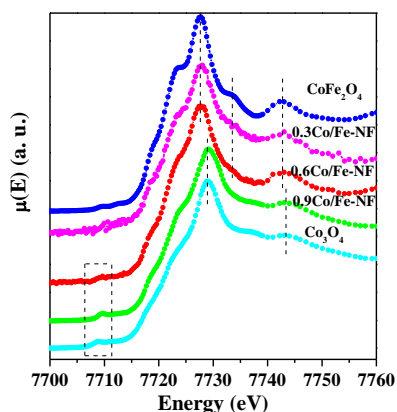
Fig. 2 Co K-edge XANES spectra of the as-prepared catalysts and reference compounds Co_3O_4 and $CoFe_2O_4$.

The morphology and microstructures of all samples were characterized by SEM and HRTEM, as displayed in Fig. 3 and Fig. S1, respectively. The top-view SEM images of Ni foam in Fig. 3(a) show that the Ni foam has interconnected macroporous structure with different diameters, and its surface exhibits uneven wrinkles of NiO with the lattice planes (220), (111), (200) and (311) exposed, as seen in Fig. 3(b) and Fig. S1(a). From Fig. 3(c) and Fig. S1(f), the thickness of the crossed Fe_2O_3 nanosheets is estimated to be ~17.1 nm, which are well-distributed and partitioned like "little rooms" on the nickel foam substrate. After supporting cobalt species, the "little rooms" consisting of Fe_2O_3 nanosheets are retained well. For the 0.3Co/Fe-NF catalyst with 0.3% of cobalt loading, only few $CoFe_2O_4$ nanoparticles with the lattice planes (222) and (220) due to the fewer loading are observed in the circled area (as shown in Fig. 3c and Fig. S1(c)). With the elevation of cobalt content to 0.6%, more $CoFe_2O_4$ nanoparticles and new Co_3O_4 nanoparticles with the lattice plane (220) (Fig. S1(d)) are simultaneously observed, which are uniformly distributed on the Fe_2O_3 nanosheets as shown in Fig. S2 (the Co/Fe active components have covered on the skeleton of inner Ni foam as observed from Fig. S3). When the content of the supported cobalt increased to 0.9%, cobalt oxide nanoparticles aggregated, which block the door of Fe_2O_3 "little rooms" and decrease the contact chance between soot and catalyst (Fig.

S1(e)). In the HRTEM images (Fig. S1) of the samples xCo/Fe-NF, $CoFe_2O_4$ and Co_3O_4 can be identified, which further proves the existence of cobalt species. Combined with the results of XRD, XANES and SEM/HRTEM, it is deduced that the as-designed multiple-component catalysts xCo/Fe-NF with special macroporous structures have been successfully prepared.
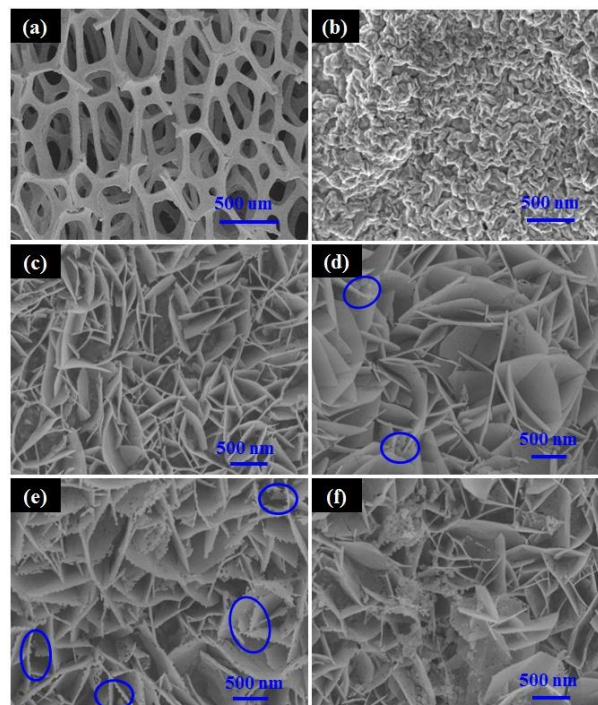
Fig. 3 SEM images illustrating the morphologies of the samples: (a-b) Ni foam, (c) Fe-NF, (d) 0.3Co/Fe-NF, (e) 0.6Co/Fe-NF, (f) 0.9Co/Fe-NF.

The mechanisms for catalyst synthesis and soot oxidation on xCo/Fe-NF are described in Scheme 1, which consists of four steps: (i) the precursor of Fe-NF was formed in the hydrothermal process; (ii) Co was loaded by a simple wet impregnation, forming xCo/Fe-NF catalysts after calcination at 500 °C; (iii) the soot particulates were captured and freely deposited on xCo/Fe-NF catalysts in SCCM, and the contact situation between soot particulates and 0.6Co/Fe-NF was shown in Fig. S4; (iv) the captured and deposited soot particulates were catalytically oxidized with the simultaneously regenerated catalyst.

Scheme 1 A schematic diagram describing the synthesis of the xCo/Fe-NF catalyst and the process for the catalytic soot oxidation.

The catalytic performance of the as-prepared catalysts for soot oxidation was evaluated by temperature-programmed oxidation (TPO) under self-capture contact mode, the results of which are shown in Fig. 4(A) and Table S2. The non-catalytic soot combustion takes place at rather high temperature; as 3DM Ni foam was used as catalyst, the soot oxidation is greatly facilitated with the ignition temperature of T_{10} at soot conversion of 10% decreases from 469 to 389 °C. After Fe_2O_3 nanosheets grow on 3DM Ni foam, the catalytic activity of Fe-NF is increased in a large scale, reflecting the much better redox property of the Fe_2O_3 nanosheets. Furthermore, the Fe-NF supported Co catalysts still show the improved catalytic activity, giving the lower T_{10}/T_{50} temperatures and higher CO_2 selectivity, especially for the 0.6Co/Fe-NF whose catalytic activity of T_{50} (382 °C) is as good as that of noble metal Pt-based catalyst.[36,37] On the one hand, the Co oxide itself is a good oxidation catalyst, which can provide new active sites and more active oxygen species during soot oxidation; on the other hand, the interaction between Co and Fe oxides may generate new active phase such as spinel $CoFe_2O_4$, as verified by EXAFS. The penetration of Co^{2+} into the lattice of Fe_2O_3 can form $CoFe_2O_4$, which possesses larger Fe-O coordination distances for the first coordination shell as compared with Fe_2O_3, as seen in Fig. S5. So, it is inferred that the Fe-O bond in $CoFe_2O_4$ can be more easily activated during soot oxidation. The catalytic activities of the samples with different Co loading show the following order: 0.6Co/Fe-NF > 0.3Co/Fe-NF > 0.9Co/Fe-NF, indicating the existence of optimal loading for Fe_2O_3 nanosheets on the 3DM Ni foam. It is known that soot combustion is a kind of deep oxidation reaction based upon catalytic redox cycles; the performance of the catalysts largely depends on their intrinsic activity (TOF).[38] Herein, we measured the TOF values by using isothermal anaerobic titrations active sites on the catalysts. Fig. 5 shows the curves of CO_2 concentration as a function of time over Fe-NF and xCo/Fe-NF catalysts during isothermal soot combustion at 330 °C. Based on these results, the quantified values of the reaction rate, the density of active oxygen sites and the TOF values for soot oxidation at 330 °C over these catalysts are obtained, as listed in Table S3. Clearly, the TOF for the different catalysts show the following order: 0.6Co/Fe-NF > 0.9Co/Fe-NF > 0.3Co/Fe-NF > Fe-NF, which is consistent with that of catalytic activity. For the 0.3Co/Fe-NF catalyst containing less cobalt, the active sites including cobalt oxide and Co-Fe interaction phase are in small quantity. Thus, the soot particulates cannot be efficiently eliminated. For the sample 0.9Co/Fe-NF containing much more cobalt, the amount of the Co_3O_4 nanoparticles is significantly increased, which accumulated seriously and blocked the crossed macropores between Fe_2O_3 nanosheets as seen in Fig. 3(f); as a result, the sample 0.9Co/Fe-NF can hardly exhibit satisfactory performance for soot combustion. While in the catalyst 0.6Co/Fe-NF, the amount of cobalt is appropriate, the Co_3O_4 nanoparticles are uniformly distributed, and the crossed

macroporous structure is well retained, all of which makes this sample have the best performance for soot oxidation.
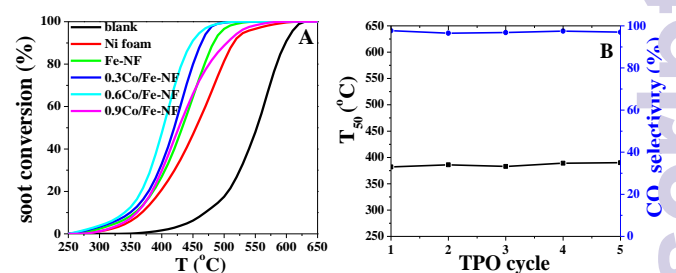
Fig. 4 (A) Soot catalytic combustion activity of the different catalysts in 300 ppm NO (or 0 ppm NO) and 5 vol. % O_2 balanced by N_2 under SCCM; (B) Stability of the 0.6Co/Fe-NF after used in 5-cycle TPO of soot in 300 ppm NO and 5% O_2 balanced by N_2.

To investigate the catalytic and structural stability of the 0.6Co/Fe-NF, five-cycle consecutive soot combustion was performed on the 0.6Co/Fe-NF catalyst and the SEM image of the spent sample was taken. The corresponding results are shown in Fig. 4(B) and Fig. S6. After five TPO cycles in 300 ppm NO and 5% O_2 balanced by N_2 under SCCM, the 0.6Co/Fe-NF catalyst still maintains high catalytic activity for soot oxidation (T_{50} = ~382 °C) and high CO_2 selectivity (~97.7%); whose nano structure and morphology nearly unchanged. These results consistently demonstrate the high stability of the catalyst 0.6Co/Fe-NF in the soot combustion reaction.
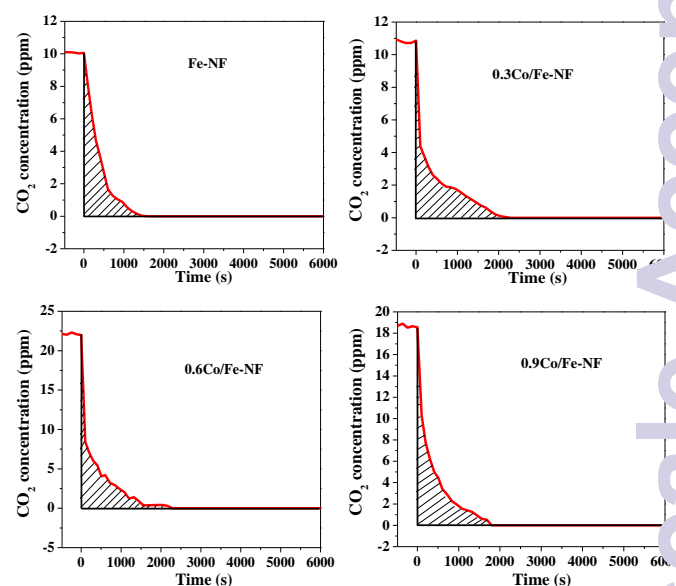
Fig. 5 The curves of CO_2 concentrations as a function of time during isothermal soot oxidation at 330 °C over the Fe-NF, 0.3Co/Fe-NF, 0.6Co/Fe-NF and 0.9Co/Fe-NF before and after removal of O_2 from the reactant feed.

It is known that for oxygen-involved oxidation reactions the property and amount of active oxygen species on catalyst surface are particularly important. To investigate the reactivity of different oxygen species on catalyst surface during soot combustion, the temperature-programmed soot oxidation over the catalysts was also performed in highly pure Ar

(99.99%) atmosphere just for a comparison with that performed in oxygen-containing atmosphere. This technique is also called soot-TPR. In this process, soot particulates can only be oxidized by the oxygen species existing on the catalyst surface such as surface adsorbed oxygen and/or surface lattice oxygen species due to the absence of gaseous oxygen in the atmosphere. The obtained soot-TPR profiles of the different catalysts are shown in Fig. 6(A). There are mainly three kinds of oxygen species, attributed to surface adsorbed oxygen O_2^- and O^- (α), surface lattice oxygen O^{2-} (β) and bulk lattice oxygen O^{2-} (γ), respectively.[1, 12, 24] Considering the mean temperature of soot combustion on these catalysts and the very high temperature for bulk oxygen activation, the surface adsorbed oxygen and surface lattice oxygen species are thought to be the main active oxygen species. Compared with those of the Fe-NF catalyst, the reduction peaks of surface oxygen species for the cobalt-containing catalysts shift to lower temperatures, suggesting the higher reactivity of the oxygen species on them. Among the xCo/Fe-NF catalysts, the 0.6Co/Fe-NF possesses the larger amounts of active oxygen species below 600 °C. These results could be well correlated with their quantified values of the active oxygen density and the TOF values.
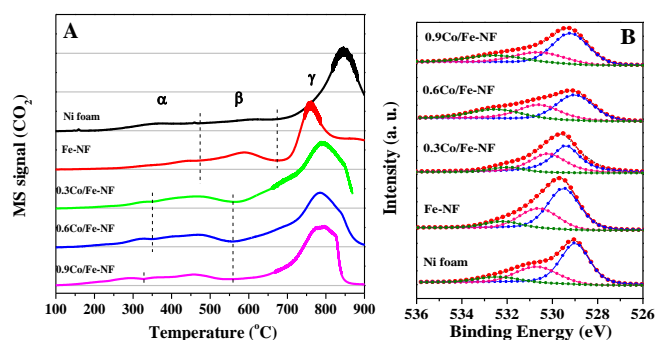
Fig. 6 (A) Soot-TPR of the Ni foam, Fe-NF, 0.3Co/Fe-NF, 0.6Co/Fe-NF and 0.9Co/Fe-NF catalysts; (B) X-ray photoelectron spectra of O1s binding energy of the prepared catalysts.

To identify the correlation between the state of Fe and catalytic performance, and further confirm the role of surface adsorbed oxygen and surface lattice oxygen in catalytic soot combustion, the XPS characterization was carried out on as-prepared samples. The binding energy of Fe ($2p_{3/2, 1/2}$) core level of the as-prepared Fe-NF is observed at 711.2 and 724 eV, respectively (Fig. S7). A satellite peak appears at ~8 eV from the main $2p_{3/2}$ level, which matches with the literature reported Fe_2O_3[39], indicating that Fe is in +3 oxidation state in the Fe-NF catalyst. After loading cobalt, the Fe ($2p_{3/2, 1/2}$) peaks shift to lower binding energy firstly and then higher binding energy, and the characteristic satellite due to the Fe^{3+} state is absent. A small satellite peak was observed at ~5 eV from the main peak, which proves the presence of Fe^{2+}. On basis of electroneutrality principle, the xCo/Fe-NF catalysts should possess oxygen vacancies.[12] After loading 0.6% cobalt, the binding energy of Fe $2p_{3/2}$ is the lowest (710.8 eV), suggesting the more Fe^{2+} and oxygen vacancies have formed, which will

be elucidated in the followed XPS results of O 1s. The O1s binding energy spectra are shown in Fig. 6(B). After deconvolution three binding energy peaks are clearly identified for all of the catalysts which appear at ~529, ~530.6 and ~532.2 eV, corresponding to surface lattice oxygen (O^{2-}), two kinds of adsorbed oxygen, namely O_2^- and O_2^{2-}, respectively.[40] Generally, the surface adsorbed oxygen is derived from the adsorption of gaseous O_2 on the oxygen vacancies of the catalysts. By simulation of the deconvoluted peaks the relative contents of different oxygen species are obtained, as listed in Table S4. Herein, the relative amounts of surface adsorbed oxygen species for the catalysts could be arranged in the same order as their activities: 0.6Co/Fe-NF > 0.9Co/Fe-NF > 0.3Co/Fe-NF > Fe-NF > Ni foam. So, it is suggested that the surface adsorbed oxygen may play an important role in catalytic soot oxidation.

It is well known that NO_2 is a stronger oxidizer than O_2.[20] In order to seek the experimental proofs of NO_2 involved in soot particulates combustion over the catalyst 0.6Co/Fe-NF, the NO_2 concentration was monitored during the temperature programmed oxidation in 300 ppm NO + 5 vol.% O_2 + N_2 in the absence or presence of soot particulates, as shown in Fig. 7(A). The NO_2 concentration over this catalyst increased with temperature rising until the thermodynamic equilibrium of the reaction (NO + 1/2O_2 ↔ NO_2) was achieved, then it decreased at higher temperatures, following the thermodynamics profile. The difference between the NO_2 concentration in the absence or presence of soot at the same temperature is defined as the reactive NO_2, which reacted with soot during the reaction. From Fig. 7(A), it is observed that over the 0.6Co/Fe-NF catalyst the profile of the reactive NO_2 has the similar tendency and temperature range with that of soot combustion. The reactive NO_2 concentration increased at the beginning of soot combustion, when the reactive NO_2 reached the maximum at ~300 °C, the rate of soot combustion did not reach the biggest value. This could be explained as follows: (1) a part of gaseous NO_2 may directly participate in soot oxidation; (2) some gaseous NO_2 may be stored in the catalysts as nitrates, which can take part in soot oxidation directly. In the higher temperature region (400-550 °C), less amount of NO_2 is desorbed into gas phase as measured by NO_2-TPD of the 0.6Co/Fe-NF (Fig. 7(B)), which suggests the direct involvement of nitrate in soot oxidation.
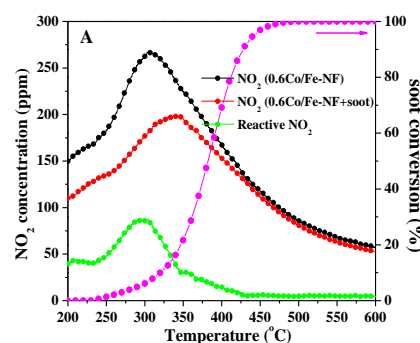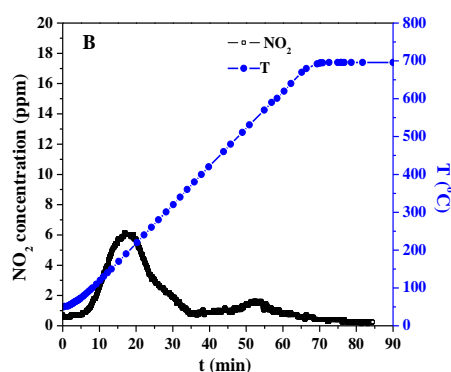
Fig. 7 (A) Concentration curves of NO_2 and soot conversion profiles for the 0.6Co/Fe-NF catalyst or the catalyst mixed with soot in the atmosphere of 300 ppm NO + 5% vol.%O_2 + N_2 and (B) NO_2-TPD profile for 0.5Co/Fe-NF, T: temperature profile.

Based upon all the results above we propose a mechanism for soot oxidation with NO and O_2 over the xCo/Fe-NF catalysts. Two reaction pathways can be summarized and shown in Scheme 2. (1) The oxygen was adsorbed and activated by Co_3O_4 nanoparticles, Fe_2O_3 nanosheets and the Fe-Co interaction phases such as $CoFe_2O_4$ spinel. The activated oxygen species can migrate from catalyst to the carbon surface through the contact site between soot and catalyst, oxidizing the soot and giving out CO or CO_2 (active oxygen catalyzed soot combustion mechanism).[41] (2) NO was oxidized to NO_2 on the catalyst surface, forming surface adsorbed species, which may migrate to solid-solid boundary and oxidize the soot; in addition, a part of NO_2 can be stored as nitrates, which can also act as an oxidizer for soot oxidation, as confirmed by NO_2-TPD (NOx-aided soot combustion mechanism).[42]

In summary, the as-prepared macroporous catalysts xCo/Fe-NF catalysts especially the 0.6Co/Fe-NF have high catalytic activities for soot combustion, which could be elucidated from the following four aspects: (1) the crossed Fe_2O_3 nanosheets and Co_3O_4 nanoparticles themselves possess strong redox ability, which makes the catalyst have high intrinsic activity; (2) the interaction between Fe and Co oxides produces new active phase such as spinel $CoFe_2O_4$, which facilitates the activation of Fe-O bond and oxygen transfer from gas phase to catalyst surface during soot combustion; (3) the Fe_2O_3 nanosheets constituted macroporous "little rooms" and the gas-permeable 3D Ni foam substrate greatly increase the soot-catalyst contact efficiency and the mass transfer rate during soot oxidation; (4) similar to noble metal catalysts, xCo/Fe-NF catalyst can efficiently catalyze NO to NO_2, which possesses higher reactivity for soot oxidation than O_2 and NO.
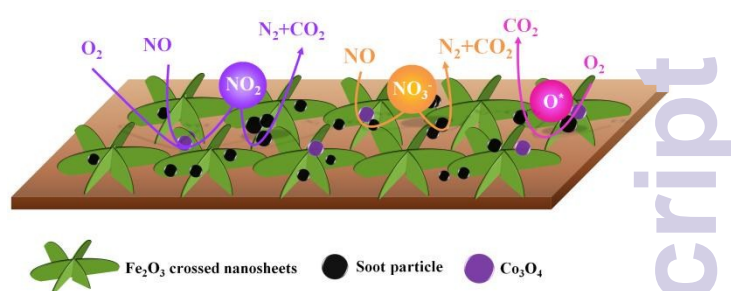
Scheme 2 Illustration of reaction mechanisms for soot combustion over the xCo/Fe-NF catalysts under self-capture contact mode.

4 Conclusions

Crossed Fe_2O_3 nanosheets supported cobalt oxide nanoparticles on three-dimensionally macroporous nickel foam substrate (xCo/Fe-NF) were successfully prepared through a facile hydrothermal route and wet impregnation method. In the composite nanomaterials, except for the Fe_2O_3 and Co_3O_4 a new interaction phase namely spinel $CoFe_2O_4$ was identified, which exhibited particularly high activity for soot oxidation due to the lengthened Fe-O bond and the increased amounts of oxygen vacancies and active oxygen species. The optimized cobalt loading in Fe-NF is 0.6 wt %. The as-prepared catalyst also exhibited high catalytic stability since the 3D macroporous Ni foam substrate and the Fe_2O_3 nanosheets constituted macroporous structure facilitate the mass and heat transfer during soot oxidation. Two reaction pathways for soot oxidation, namely the direct oxidation by the activated oxygen species via oxygen vacancies and the NOx-aided soot oxidation are revealed.

Acknowledgements

Notes and references

1   X. Guo, M. Meng, F. F. Dai, Q. Li, Z. L. Zhang, Z. Jiang, S. Zhang and Y. Y. Huang, *Appl. Catal., B*, 2013, **142**, 278.
2   S. Liu, X. D. Wu, D. Weng, M. Li and R. Ran, *ACS Catal.*, 2015, **5**, 909.
3   E. Aneggi, N. J. Divins, C. Leitenburg, J. Liorca and A. Trovarelli, *J. Catal.*, 2014, **312**, 191.
4   R. Kimura, J. Wakabayashi, S. P. Elangovan, M. Ogura, and T. Okubo, *J. Am. Chem. Soc.*, 2008, **130**, 12844.
5   Y. F. Yu, M. Meng and F. F. Dai, *Nanoscale*, 2013, **5**, 904.
6   M. E. Gálvez, S. Ascaso, P. Stelmachowski, P. Legutko, A. Kotarba, R. Moliner and M. J. Lázaro, *Appl. Catal., B,* 2014, **152**, 88.
7   Y. F. Yu, J. L. Ren, D. S. Liu and M. Meng, *ACS Catal.*, 2014, **4**, 934.
8   A. Bueno-López, *Appl. Catal., B*, 2014, **146**, 1.

9   B. R. Stanmore, J. F. Brilhac, P. Gilot, *Carbon*, 2001, **39**, 2247.

10 Y. C. Wei, Z. Zhao, J. Liu, C. M. Xu, G. Y. Jiang and A. J. Duan, *Small*, 2013, **23**, 3957.

11 G. Z. Zhang, Z. Zhao, J. Liu, G. Y. Jiang, A. J. Duan, J. X. Zheng, S. L. Chen and R. X. Zhou, *Chem. Commun.*, 2010, **46**, 457.

12 Z. Q. Li, M. Meng, Y. Q. Zha, F. F. Dai, T. D. Hu, Y. Xie and J. Zhang, *Appl. Catal., B*, 2012, **121**, 65.

13 P. G. Harrison, I. K. Ball, W. Daniell, P. Lukinskas, M. Céspedes, E. E. Miró and M. A. Ulla, *Chem. Eng. J.*, 2003, **95**, 47.

14 N. Guillén-Hurtado, A. García-García and A. Bueno-López, *Appl. Catal., B*, 2015, **174**, 60.

15 D. Fino, N. Russo, G. Saracco and V. Specchia, *J. Catal.*, 2006, **242**, 38.

16 E. Aneggi, D. Wiater, C. de Leitenburg, J. Llorca and A. Trovarelli, *ACS Catal.*, 2014, **4**, 172.

17 X. X. Zhou, H. R. Chen, G. B. Zhang, J. Wang, Z. G. Xie, Z. L. Hua, L. X. Zhang and J. L. Shi, *J. Mater. Chem. A*, 2015, **3**, 9745.

18 Y. C. Wei, J. Liu, Z. Zhao, Y. S. Chen, C. M. Xu, A. J. Duan, G. Y. Jiang and H. He, *Angew. Chem.*, 2011, **50**, 2326.

19 R. Ramdas, E. Nowicka, R. Jenkins, D. Sellick, C. Davies and S. Golunski, *Appl. Catal., B*, 2015, **176**, 436.

20 Y. C. Wei, J. Liu, Z. Zhao, A. J. Duan and G. Y. Jiang, *J. Catal.*, 2012, **287**, 13.

21 Y. C. Wei, J. Liu, Z. Zhao, A. J. Duan, G. Y. Jiang, C. M. Xu, J. S. Gao, H. He and X. P. Wang, *Energy Environ. Sci.*, 2011, **4**, 2959.

22 J. F. Xu, J. Liu, Z. Zhao, C. M. Xu, J. X. Zheng, A. J. Duan and G. Y. Jiang, *J. Catal.*, 2011, **282**, 1.

23 J. L. Ren, Y. F. Yu, F. F. Dai, M. Meng, J. Zhang, L. Zheng and T. D. Hu, *Nanoscale*, 2013, **5**, 12144.

24 C. M. Cao, Y. X. Zhang, D. S. Liu and M. Meng, *Small*, 2015, **11**, 3659.

25 C. Guan, J. P. Liu, C. W. Cheng, H. X. Li, X. L. Li, W. W. Zhou, H. Zhang and H. J. Fan, *Energy Environ. Sci.*, 2011, **4**, 4496.

26 G. L. Wang, D. X. Cao, C. L. Yin, Y. Y. Gao, J. L. Yin and L. Cheng, *Chem. Mater.*, 2009, **21**, 5112.

27 G. Q. Zhang and X. W. Lou, *Adv. Mater.*, 2013, **25**, 976.

28 D. Lei, M. Zhang, B. H. Qu, L. B. Chen, Y. G. Wang, E. D. Zhang, Z. Xu, Q. H. Li and T. H. Wang, *Nanoscale*, 2012, **4**, 3422.

29 N. Yan, X. Z. Fu, J. L. Luo, K. T. Chuang and A. R. Sanger, J. Power Sources, 2012, **198**, 164.

30 S. X. Cai, D. S. Zhang, L. Y. Shi, J. Xu, L. Zhang, L. Huang, H. R. Li and J. P. Zhang, Nanoscale, 2014, **6**, 7346.

31 K. Cheng, F. Yang, G. L. Wang, J. L. Yin and D. X. Cao, J. Mater. Chem. A, 2013, **1**, 1669.

32 Y. Liu, J. Xu, H. R. Li, S. X. Cai, H. Hu, C. Fang, L. Y. Shi and D. S. Zhang, J. Mater. Chem. A, 2015, **3**, 11543.

33 P. Darcy, P. D. Costa, H. Mellottée, J. M. Trichard and G. Djéga-Mariadassou, *Catal. Today*, 2007, **119**, 252.

34 Z. L. Zhang, D. Han, S. J. Wei and Y. X. Zhang, *J. Catal.*, 2010, **276**, 16.

35 G. Aquilanti, A. Cognigni and M. Anis-ur-Rehman, *J. Supercond. Nov. Magn.*, 2010, **24**, 659.

36 L. Castoldi, R. Matarrese, L. Lietti and P. Forzatti, *Appl. Catal., B.* 2006, **64**, 25.

37 R. Matarrese, L. Castoldi, L. Lietti and P. Forzatti, Catal. Today, 2008, **136**, 11.

38 P. F. Zhu, J. Li, S. F. Zuo and R. X. Zhou, *Appl. Surf. Sci.*, 2008, **255**, 2903.

39 A. Gupta, A. Kumar, U. V. Waghmare and M. S. Hegde, *Chem. Mater.*, 2009, **21**, 4880.

40 Y. C Wei, Z. Zhao, T. Li, J. Liu, A. J. Duan and G. Y. Jiang, *Appl. Catal., B*, 2014, **146**, 57.

41 E. Baumgarten and A. Schuck, *Appl. Catal.*, 1988, **37**, 247.

42 G. Mul, F. Kapteijn, C. Doornkamp, and J. A. Moulijn, *J. Catal.*, 1998, **179**, 258.